Skin image illumination modeling and chromophore identication for melanoma diagnosis

Zhao Liu, Josiane Zerubia

Skin image illumination modeling and chromophore identification for melanoma diagnosis

Zhao Liu and Josiane Zerubia
INRIA, Ayin Research Team, 06902 Sophia Antipolis, Cedex, France

E-mail: zhao.liu@inria.fr and josiane.zerubia@inria.fr

Abstract: The presence of illumination variation in dermatological images has a negative impact on the automatic detection and analysis of cutaneous lesions. This paper proposes a new illumination modeling and chromophore identification method to correct lighting variation in skin lesion images, as well as to extract melanin and hemoglobin concentrations of human skin, based on an adaptive bilateral decomposition and a weighted polynomial curve fitting, with the knowledge of a multi-layered skin model. Different from state-of-the-art approaches based on the Lambert law, the proposed method, considering both specular reflection and diffuse reflection of the skin, enables us to address highlight and strong shading effects usually existing in skin color images captured in an uncontrolled environment. The derived melanin and hemoglobin indices, directly relating to the pathological tissue conditions, tend to be less influenced by external imaging factors and are more efficient in describing pigmentation distributions. Experiments show that the proposed method gave better visual results and superior lesion segmentation, when compared to two other illumination correction algorithms, both designed specifically for dermatological images. For computer-aided diagnosis of melanoma, sensitivity achieves 85.52% when using our chromophore descriptors, which is 8~20% higher than those derived from other color descriptors. This demonstrates the benefit of the proposed method for automatic skin disease analysis.

Keywords: adaptive bilateral decomposition, weighted polynomial curve fitting, melanin identification, hemoglobin identification, skin disease analysis.

1. Introduction

Skin colour is an important characteristic for accurate diagnosis and grading of cutaneous lesions by experienced dermatologists in clinical practice. For example, the presence of multiple colour shades and pigmentation asymmetry within lesions often indicates a high risk of developing malignant melanoma (MM) (Friedman *et al* 1985). However, visual perception of skin colour is not only credited to major chromophores (melanin and hemoglobin) underneath the skin surface, but is also affected by external illumination and spectral responses of imaging detectors. Skin colour representation in a specific colour space (e.g. RGB and its transformations) is not a genuine physical quantity. It derives from colour matching functions of human visual system (Wandell 1995). It sometimes fails to provide precise information about the concentrations of cutaneous chromophores, and is easily influenced by external imaging factors. For example, figure 1 shows a MM image, whose pigmentation information is partially concealed by illumination artifacts. As a result, conventional colourimetry may not properly describe the underlying histological content of skin and tend to yield less trustworthy results when colourimetry is applied directly to skin disease analysis.

A number of studies have been developed for non-invasive assessment of melanin and hemoglobin on skin lesion images. Claridge *et al* (2003) proposed a sophisticated multilayered skin model based on Kubelka-Munk theory for extracting epidermal and dermal melanin, blood, and collagen thickness using multispectral skin data. Yamamoto *et al* (2008) applied a much simple three-layered skin model based on the Lambert law, and calculated melanin index and erythema index in RGB skin images. But Claridge's

approach requires multispectral images, which are not always available in clinical practice; while Yamamoto's algorithm is reported sensitive to imaging circumstantial conditions, as there is no illumination-modeling step to correct external imaging factors in their method.

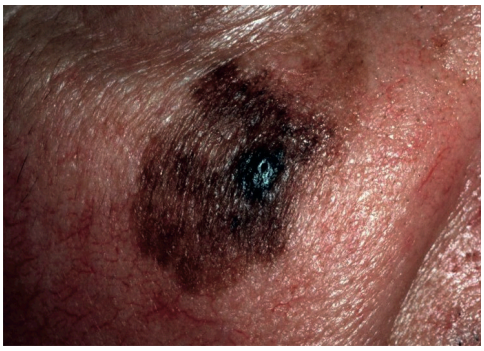

Figure 1 A melanoma image from a public database (Galderma 2014) with obvious highlight and shading effects.

Tsumura *et al* (2003) removed shading effects by a colour vector analysis in optical density domain, and applied independent component analysis (ICA) on RGB skin images to separate average concentrations of melanin and hemoglobin. Similarly, Madooei *et al* (2012) introduced extra imaging factors (e.g. shading, sensor characteristics) to a diffuse reflection skin model and cancelled out their influences by directly dividing two spectral responses in original lesion images. Then they also applied ICA approach on the post-processed RGB channels for extracting chromophore densities. These methods show efficiency for shading removal in skin colour images, and their chromophore descriptors are useful for characterizing cutaneous pigmentation for MM diagnosis. However, ICA-based methods are only responsible for separating a skin image into two independent components, and do not associate the knowledge of the absorbance spectrum. This results in ambiguities when differentiating melanin from hemoglobin.

All the above methods, either specified (Tsumura *et al* 2003, Madooei *et al* 2012) or not included (Claridge *et al* 2003, Yamamoto *et al* 2008) an illumination correction function, refer to human skin as a merely diffuse reflectance surface. They ignore the specular reflection at the air-skin interface. But this component is generally believed as the cause of highlight and its effect changes with viewing direction. Accordingly these existing methods will fail to address highlight effects in skin lesion images captured under non-polarized conditions.

This paper, considering human skin as a specular + diffuse reflectance model, proposes a novel illumination correction and chromophore identification scheme on dermatological images following three steps. First, specular reflection is separated from diffuse reflection through specular pixel localization and a B-spline image interpolation. Second, the resulting diffuse image is decomposed into a base layer and a detail layer. The base layer, having low frequency illumination and shading effects, is approximated by polynomial curve fitting taking an initial illumination map from an adaptive bilateral filter as a prior. The detail layer, containing high frequency chromophore reflectance, is calculated by subtracting the base layer from the diffuse spectral band in a logarithmic form. Finally, incorporating the knowledge of chromophore absorption characteristics, melanin density and hemoglobin density are well identified using detail layers from different spectral channels.

Experiments show that the proposed method is able to address highlight and strong shading effects in dermatological photographs of large dynamic range intensity. The derived chromophore descriptors, more efficient in describing pigmentation distributions of skin, demonstrate to be useful for improving the automatic diagnosis of melanoma.

2. A Multiple-Layered Skin Model

Human skin can be simplified as a thin structure with distinctive multiple layers, which correspond to melanin-rich epidermis, hemoglobin-rich dermis, and subcutis with collagen and fat (Tsumura *et al* 2003). Based on this multilayered model, previous methods (Tsumura *et al* 2003, Madooei *et al* 2012) use Lambert law to characterize skin radiance provided that there is little specular reflection at the skin surface. This diffuse reflectance model is efficient in modeling skin images captured under polarized lighting (e.g. dermoscopy images), but it is not appropriate to handle cutaneous images illuminated under uncontrolled imaging settings. Therefore, this study considers skin as a specular reflection and diffuse reflection model in figure 2, and skin image intensity I at pixel (x, y) and wavelength λ can be written as a combination of specular reflection I_s and diffuse reflection I_d as:

$$\begin{aligned} I_\lambda(x,y) &= I_{s,\lambda}(x,y) + I_{d,\lambda}(x,y) \\ &= Q_\lambda \left[k_s E_{s,\lambda}(w_s(x,y))^\alpha + k_d E_{d,\lambda} w_d(x,y) e^{-\left(\mu_{m,\lambda} l_{m,\lambda} c_m(x,y) + \mu_{h,\lambda} l_{h,\lambda} c_h(x,y)\right)} \right] \end{aligned} \quad (1)$$

where Q_λ stands for sensor characteristics. k_s and k_d are specular reflection constant and diffuse reflection constant, respectively. $E_{s,\lambda}$ and $E_{d,\lambda}$ are intensities of specular and diffuse components of light source. w_s is the specular factor giving rise to highlight, which is the dot product between viewer direction and specular reflection direction. α is a material relevant constant, which assigns a large value for a smooth surface while a small value for a rough one. w_d is the wavelength-independent shading variable due to scene geometry, which is the dot product between surface normal and lighting direction. $\mu_{m,\lambda}$ and $\mu_{h,\lambda}$ are wavelength-dependent absorptive coefficients of melanin and hemoglobin, respectively. $l_{m,\lambda}$ and $l_{h,\lambda}$ are the accumulated path lengths of photons in epidermis and dermis layers. c_m and c_h are densities of melanin and hemoglobin in a sampled volume of skin.

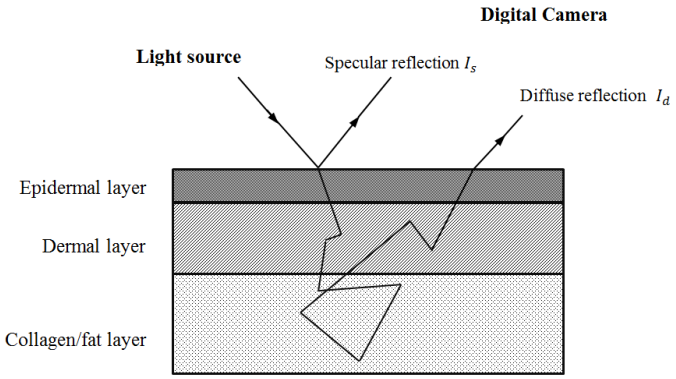

Figure 2 A three-layered skin reflectance model.

3. Methods

3.1 Specular Reflection and Diffuse Reflection Separation

Yang et al (2010) estimate the maximum diffuse chromaticity of the specular pixels by apply- ing bilateral filter to the maximum fraction of the color components in original image, such that the maximum diffuse chromaticity can be propagated from the diffuse pixels to the specu- lar pixels. This method works well for removing specular reflection on images of man-made objects, which have smooth surfaces and distinctive hue colors. But it poses much difficulty when applied directly on texture-rich skin images. This is because human skin has areas shar- ing similar hue values but different saturations. Surface texture in these areas will be filtered out as the specular component. As a result, the diffuse image becomes blurred, and part of the skin texture information, having diagnostic importance, is lost. These

drawbacks can be clearly detected in the diffuse image of an MM example derived from (Yang et al 2010) in figure 3(c).

In this study, we apply Yang's method to localize candidate specular component first. Then the highlight areas are decided by selecting pixel intensity larger than a threshold, which is set to 0.25 times of the maximum intensity in candidate specular image. Compared to the candi- date specular component (figure 3(a)), the surface texture is greatly reduced in the specular image after thresholding (figure 3(b)).

In principle, the diffuse reflection can be obtained by subtracting the specular component from original skin image. But direct subtraction may yield some fake intensity pixels, visible as dark spots, in the derived diffuse image (figure 3(c)). This is because the image intensity of these pixels is dominated by specular reflection, while diffuse reflection is largely missing due to local surface smoothness and observation direction. Subtraction results in small pixel intensity in all the RGB channels, but not the real diffuse chromaticity. This undesired effect becomes worse when specular reflection is strong.

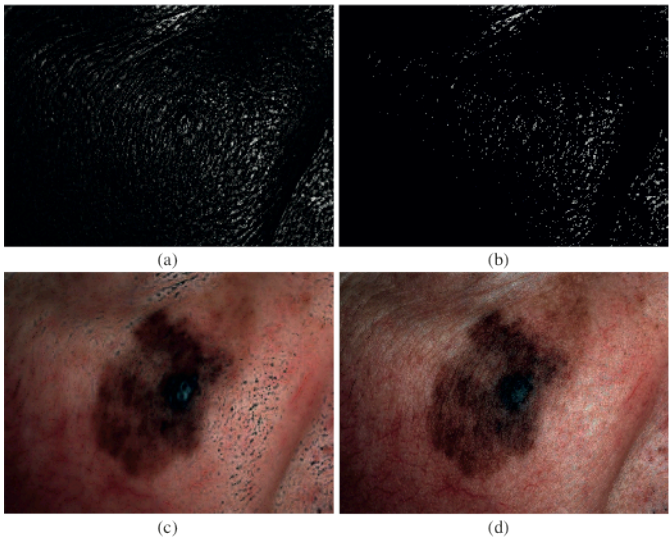

Figure 3 Specular reflection removal in skin image, taking the MM in figure 1 for example. (a) Candidate specular reflection by Yang's method (Yang *et al* 2010). (b) Specular reflection after thresholding. (c) Blurred diffuse image by subtracting figure 3(a) from figure 1, having fake intensity pixels visible as dark spots. (f) Diffuse image by our method using a B-spline image interpolation.

To circumvent this problem, the diffuse chromaticity of the detected specular pixels is obtained by a B-spline interpolation (Thévenaz *et al* 2000) using neighboring non-specular points as:

$$\begin{cases} I_{d,\lambda}(x,y) = I_{\lambda}(x,y) & (x,y) \notin M_s \\ I_{d,\lambda}(x,y) = \dfrac{K_{rx}\left[I_{\lambda,\Omega_{(x,y)}} * W_{\Omega_{(x,y)}}\right]K'_{ry}}{K_{rx}W_{\Omega_{(x,y)}}K'_{ry}} & (x,y) \in M_s \end{cases}, \quad K_{rx} = \begin{cases} \frac{2}{3} - \frac{1}{2}|rx|^2(2-|rx|) & 0 \le |rx| < 1 \\ \frac{1}{6}(2-|rx|)^3 & 1 \le |rx| < 2 \\ 0 & 2 \le |rx| \end{cases} \tag{2}$$

where M_s is a set of specular pixels after thresholding. $\Omega_{(x,y)} = \{(i,j)\}$ is the neighborhood of pixel (x, y) where $\left\{rx = \left|\frac{x-i}{4}\right| < 2, ry = \left|\frac{y-j}{4}\right| < 2\right\}$. $W_{\Omega_{(x,y)}}$ is a matrix of $\Omega_{(x,y)}$ assigning 1 to non-specular pixels and 0 to specular pixels. K_{rx} and K_{ry} are vectors of interpolation coefficients in x- and y-directions. Figure 3(d) shows the diffuse reflection image derived from our method.

3.2 Decomposition of Diffuse Reflection Image

After specular reflection removal, the remaining diffuse reflection can be formulated by a linear combination of chromophore coefficients, optical parameters of light source, and effects of scene geometry in an inverse logarithmic form as:

$$\log_e I_{d,\lambda}(x,y) = \left(\mu_{m,\lambda} l_{m,\lambda} c_m(x,y) + \mu_{h,\lambda} l_{h,\lambda} c_h(x,y)\right) - \log_e Q_\lambda - \log_e E_{d,\lambda} - \log_e w_d(x,y) \tag{3}$$

3.2.1 Initial Illumination Approximation. Bilateral filter, firstly proposed in (Tomasi and Manduchi 1998), was developed for image denoising meanwhile preserving important edges and features. It extends the concept of Gaussian smoothing through a weighted average process of neighboring pixels. In this study, bilateral filter is applied to diffuse skin image $I_{d,\lambda}$ to estimate the initial illumination map. The output image $log_e I'_{d,\lambda}$ after filtering at pixel (x, y) and wavelength λ is given as:

$$\begin{aligned}
&\log_e I'_{d,\lambda}(x,y) = \frac{1}{A}\sum_{(p,q)\in\Omega_{(x,y)}} \varphi\big((p,q),(x,y)\big)\Phi\big(\log_e I_{d,\lambda}(p,q),\log_e I_{d,\lambda}(x,y)\big)\log_e I_{d,\lambda}(p,q) \\
&= \left[-\log_e Q_\lambda - \log_e E_{d,\lambda}\right] + \left[\frac{1}{A}\sum_{(p,q)\in\Omega_{(x,y)}} \varphi\big((p,q),(x,y)\big)\Phi\big(\log_e I_{d,\lambda}(p,q),\log_e I_{d,\lambda}(x,y)\big)\big(\mu_{m,\lambda} I_{m,\lambda} c_m(p,q) + \mu_{h,\lambda} I_{h,\lambda} c_h(p,q) - \log_e w_d(p,q)\big)\right]
\end{aligned} \tag{4}$$

where (p, q) belongs to the neighborhood $(\Omega_{(x,y)})$ of pixel (x, y), and A is a normalizing constant. The first term of the above equation refers to illumination information, which is a function of λ. The second term contains chromophore reflectance $(\mu_\lambda l_\lambda c)$ and shading effects (w_d), whose contributions in $log_e I'_{d,\lambda}$ are controlled by a spatial function φ and a range function Φ, defined as Gaussian kernels in this study:

$$\varphi\big((p,q),(x,y)\big)\Phi\big(\log_e I_{d,\lambda}(p,q),\log_e I_{d,\lambda}(x,y)\big) = \exp\left(-\frac{\|(p,q)-(x,y)\|^2}{2\sigma_1^2}\right)\exp\left(-\frac{\left\|\log_e I_{d,\lambda}(p,q)-\log_e I_{d,\lambda}(x,y)\right\|^2}{2\sigma_2^2}\right) \tag{5}$$

Considering that shading is normally a low frequency component which changes gradually across large skin areas, high frequency chromophore elements can be smoothed out by selecting relatively large spatial (σ_1) and intensity (σ_2) standard deviations (SD), whose values depend on specific applications. Subtracting $log_e I'_{d,\lambda}$ from $log_e I_{d,\lambda}$, intrinsic chromophore information can be obtained. We then embed this bilateral filtering in an iterative process such that chromophore reflectance will iteratively propagate till the difference between images before and after filtering is smaller than a threshold t for each pixel. In this study, t = 0.01*$\log_e(255)$ ≈ 0.05, which means 1% of the overall image intensity range. The iterative process is summarized as Algorithm-1 below.

Algorithm-1: Initial illumination approximation

Input: $I_{loop} = log_e I_{d,\lambda}$

Repeat: (1) Apply bilateral filter on I_{loop}, store filtered image I'_{loop}.

(2) Compute propagated chromophore reflectance $I_c = I_c + I_{loop} - I'_{loop}$, and the remaining component after this iteration $I_{remain} = log_e I_{d,\lambda} - I_c$.

(3) If $\left\|I'_{loop} - I_{loop}\right\| < t$ for every pixel, step outside loop. Otherwise $I_{loop} = I_{remain}$, and repeat steps (1)~(3).

Output: $\mathcal{L}_{ini,\lambda} = I_{remain}$

It should be noted that the goodness of illumination approximation by standard bilateral filter depends on the selection of σ_1 and σ_2 for individual images. Large spatial and intensity SDs may make the normal skin areas overly smoothed, and part of the shading effects fail to be removed; while small SDs could lead to poor illumination estimation, where overall lesion areas appear as shading in the estimated illumination map. As a result, the contrast between lesion areas and surrounding normal skin was greatly reduced in the corrected image.

In order to cope with this problem, we take image intensity gradients as reference to make the spatial and range standard deviations adaptive to each pixel:

$$\sigma_{1,\lambda}(x,y) = \min(Rg_x, Rg_y) * G_\lambda(x,y) \quad , \quad \sigma_{2,\lambda}(x,y) = Rg_{I_{d,\lambda}} * G_\lambda(x,y) \tag{6}$$

$$G_\lambda(x,y) = 1 - \exp\left(-\frac{\left\| \nabla I_{d,\lambda}(x,y) \right\|}{2\sigma_G^2} \right) \tag{7}$$

where Rgx and Rgy are the width and height of the image, and RgId,λ is the maximum intensity value in the diffuse image of channel λ. G_λ is a monotonically increasing function of image intensity gradient $\nabla I_{d,\lambda}$, and σ_G controls increasing rate of function G_λ. Hence pixels of large intensity gradients, corresponding to lesion areas, are assigned large SDs; whereas pixels of small intensity gradients, referring to homogeneous normal skin, are given small σ_1 and σ_2 values (figure 4(d)). Using this adaptive bilateral filter, shading effect is kept in the filtered image; meanwhile chromophore components are gradually smoothed out during each iteration.

Figure 4(e) shows the illumination approximation of the MM example in figure 3, derived from Algorithm-1 applying the proposed adaptive bilateral filter. It is obvious that shading effects on the left are well preserved in the RGB channels due to the selection of small smoothing parameters, while most of the chromophore information is removed as high-frequency elements by strong averaging process. But varied SDs at different pixels make the illumination estimation $\mathcal{L}_{\text{ini}}$ unnatural and less homogeneous. Thus a polynomial curve fitting is subsequently introduced to generate the final illumination image.

3.2.2 Final Illumination Modeling. Polynomial function f in (8) is applied as a parametric modeling of lighting variation. Three sets of polynomial orders $(nx, ny) \in N$, corresponding to horizontal shading (2,1), vertical shading (1,2), and radial shading (2,2), are considered in this study. Our objective is to optimize the polynomial coefficients ρ in the model through minimizing the cost function (9) using the initial illumination estimation $\mathcal{L}_{ini}$ as a prior.

$$f(x,y,nx,ny) = \begin{cases} \sum_{w=v}^{nx} \rho_{wv} x^{w-v} \sum_{v=0}^{ny} y^v & nx \geq ny \\ \sum_{v=w}^{ny} \rho_{wv} y^{v-w} \sum_{w=0}^{nx} x^w & nx < ny \end{cases} \tag{8}$$

$$f = \underset{(nx,ny)\in N}{\arg\min} \left(\sum_{(x,y)\in I} \varpi_\lambda(x,y) \left\| \mathcal{L}_{ini,\lambda}(x,y) - f(x,y,nx,ny) \right\| \right) \tag{9}$$

where ϖ_λ is a monotonically decreasing function defined as $\varpi_\lambda = \beta^{\|\nabla I_{d,\lambda)}\|}$ with β=0.01 as a constant. It assigns relatively smaller weights to pixels in skin lesion areas with large intensity gradient, so that normal skin areas give greater contribution in calculating the final illumination map. As shown in figure 5, the introduction of weight ϖ_λ enables the parameter σ_G in (7) to be chosen in a larger range without greatly influencing the final illumination estimation. In this study, we set $\sigma_G = 0.3$ throughout the work.

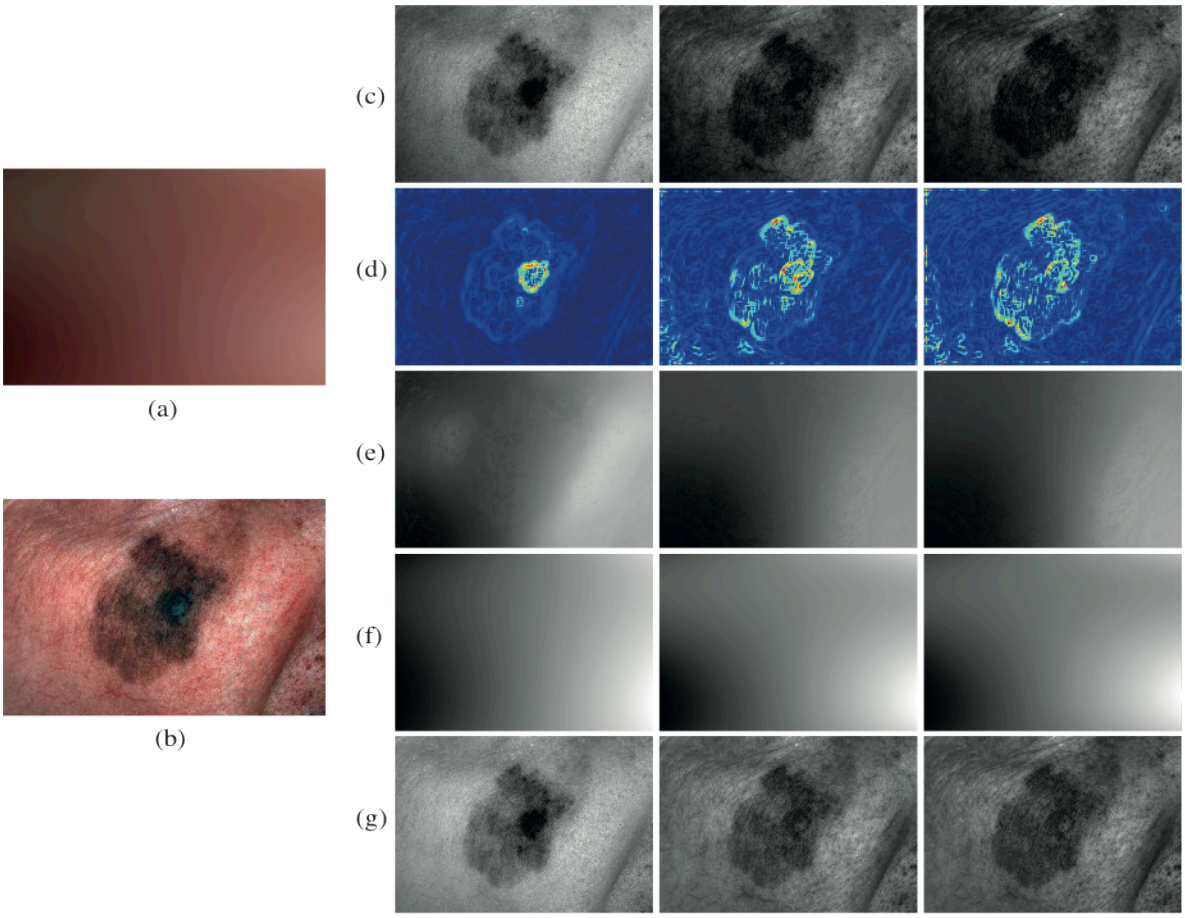

Figure 4 Base layers and detail layers of the MM image in figure 1. (a) Illumination component. (b) Corrected image after illumination modeling by the proposed method. (c) Spectral bands of diffuse reflection image. (d) Intensity gradient expressed by the monotonically increasing function G_λ with $\sigma_G = 0.3$. Blue color refers to small G_λ value, while red color stands for large one. (e) Initial illumination approximation $\mathcal{L}_{\text{ini}}$ by the adaptive bilateral filtering. (f) Base layers, and (g) Detail layers after polynomial curve fitting, taking $\mathcal{L}_{\text{ini}}$ as a prior. For comparison with the original spectral bands in (c), $\mathcal{L}_{\text{ini}}$, I_{base} and I_{detail} are shown in the exponential form. 1st – 3rd columns: Red, Green and, Blue channels, respectively.

Subtracting the final illumination estimation from the diffuse reflection component, a skin image can be decomposed into a base layer I_{base} having low frequency imaging factors, and a detail layer I_{detail} containing chromophore reflectance:

$$I_{base,\lambda}(x,y) = -\log_e Q_\lambda - \log_e E_{d,\lambda}(x,y) - \log_e w_d(x,y) \tag{10}$$

$$I_{\text{detail},\lambda}(x,y) = \mu_{m,\lambda} l_{m,\lambda} c_m(x,y) + \mu_{h,\lambda} l_{h,\lambda} c_h(x,y) \tag{11}$$

We will write $I_{base,\lambda}(x,y)$, $I_{detail,\lambda}(x,y)$, $c_m(x,y)$, and $c_h(x,y)$, as $I_{base,\lambda}$, $I_{detail,\lambda}$, c_m, and c_h for simplicity hereafter.

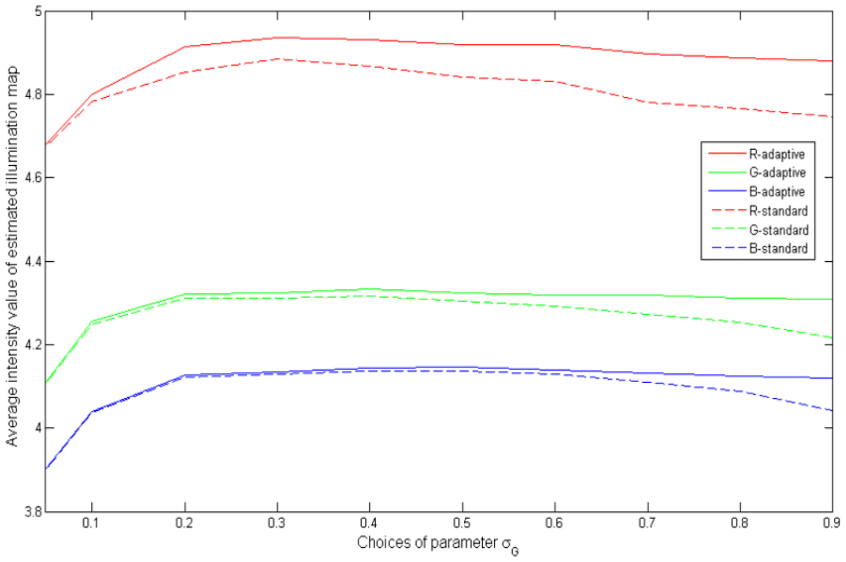

Figure 5 Average intensity values of estimated illumination map with the change of parameter σ_G, calculated with and without the introduction of weight ϖ_λ in (8). The average intensity values are stable in the range of $\sigma_G \in [0.2\ 0.9]$, if weight ϖ_λ is applied; but they become fluctuated without ϖ_λ. Numerically, when $\sigma_G \in [0.2\ 0.9]$, the maximum differences of intensity in the exponential form (0~255 range) are 7.57, 1.83, 1.60 for R, G, and B channels respectively with the assignment of weight ϖ_λ; while the differences increased to 17.35, 7.06, and 5.61 without it.

From figure 4, the resultant base layers, responsible for low frequency component across large smooth regions, match with the varied illumination information in the original spectral bands at different wavelengths. The corresponding detail layers show pigmentation in large skin regions with little illumination influence. In addition, it is worth noting that the exact degree of pigmentation in the detail layers greatly changes among the RGB channels. This is because the absorbance spectrum of melanin and hemoglobin varies with wavelength. Thus the diffuse reflectance of skin in a specific spectral band can be considered as an effect attributed to particular chromophores. Therefore, melanin index and hemoglobin index can be calculated.

3.3 Melanin Index and Hemoglobin Index Estimation

As shown in figure 6, melanin, the major pigmentation chromophore, effectively absorbs light from 400nm to 1,000nm; whereas oxyhemoglobin and deoxyhemoglobin, the major blood chromophores, both greatly absorb light around 450nm and 570nm. Due to the increased spectrum attenuation of hemoglobin, the absorption at longer wavelength light (>620nm) is dominated by melanin, whilst that of hemoglobin is negligible. Associating chromophore absorbance with the spectral responses of conventional RGB cameras, image intensity in red channel (~650nm) is primarily attributed to melanin concentration, while those of green (~550nm) and blue (~450nm) channels are the joint effects of melanin and hemoglobin simultaneously. The detail layers of skin image intensity in the RGB channels can then be expressed as:

$$I_{\mathrm{det}ail,r} = \mu_{m,r} l_{m,r} c_m \tag{12}$$

$$I_{\mathrm{det}ail,g} = \mu_{m,g} l_{m,g} c_m + \mu_{h,g} l_{h,g} c_h \tag{13}$$

$$I_{\mathrm{det}ail,b} = \mu_{m,b} l_{m,b} c_m + \mu_{h,b} l_{h,b} c_h \tag{14}$$

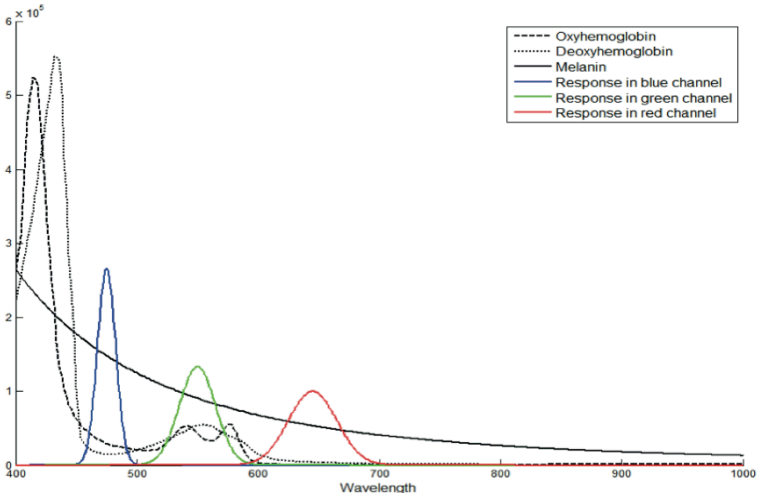

Figure 6. Spectral absorption of major chromophores from 400nm to 1,000nm based on the published data (Jacques 1998), and their relation with spectral responses of conventional RGB digital cameras.

Based on the previous publications about absorptive coefficients and light penetration lengths into human skin (Jacques 1998, Keller *et al* 2001), the melanin density and hemoglobin density can be estimated:

$$\begin{pmatrix} c_m \\ c_h \end{pmatrix} = \begin{pmatrix} \mu_{m,r} l_{m,r} & 0 \\ \mu_{m,g} l_{m,g} & \mu_{h,r} l_{h,r} \\ \mu_{m,b} l_{m,b} & \mu_{h,r} l_{h,r} \end{pmatrix}^{-1} \begin{pmatrix} I_{detail,r} \\ I_{detail,g} \\ I_{detail,b} \end{pmatrix} \tag{15}$$

$$= \begin{pmatrix} 0.4313 & -0.229 & 0.9456 \\ -0.2349 & 0.8262 & -0.3451 \end{pmatrix} * \begin{pmatrix} I_{detail,r} \\ I_{detail,g} \\ I_{detail,b} \end{pmatrix}$$

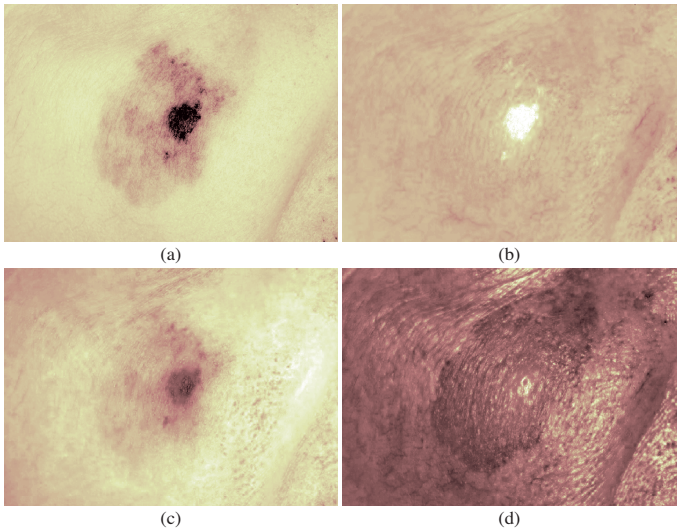

Figure 7 Melanin and hemoglobin concentrations calculated by different algorithms. (a) MI and (b) HI derived from the proposed approach. (c) First and (d) second independent components by the ICA method (Madooei *et al* 2012).

In this study, the melanin index is defined as $MI = c_m$ and the hemoglobin index is $HI = c_h$. Figure 7 shows the MI and HI of the MM image in figure 3. This example has both dark brown/black (lesion) and reddish (vessels) responses, reflecting the underlying melanin and hemoglobin densities respectively. The MI mapping from our method successfully addresses the shading effects, giving apparent contrast between blackish areas within MM and surrounding healthy skin. The corresponding HI mapping has little highlight effects, and reveals the capillaries that are concealed by illumination in that of the ICA approach (Madooei *et al* 2012). All these should lead to more accurate results in automatic skin disease analysis.

4. Experiments and Results

4.1 Experiment Data and Setup

For algorithm evaluation, a number of 258 conventional RGB skin lesion images, including 76 MMs, 182 benign nevi (BN), are collected from two public databases (Galderma 2014, Diepgen *et al* 2014). Of these lesions, 154 were reported to be excised and examined by histopathology, giving 76 MMs and 78 BN diagnosed as 34 Dysplastic nevi, 30 Common Acquired nevi, 8 Blue nevi, 5 Spitz nevi, and 2 Seborrheic Keratosis. The remaining 104 lesions did not undertake excision biopsy due to no evidence of malignancy under clinical examinations.

Automatic skin lesion segmentation and computer-aided melanoma diagnosis are performed to show the usefulness of the proposed method in skin disease analysis. In lesion segmentation experiment, images after illumination modeling by our approach are first visually compared with the results from two other illumination correction methods (Cavalcanti and Scharcanski 2011, Glaister *et al* 2013). Both were developed specifically for skin image analysis. Then automatic lesion segmentation is performed as quantitative analysis, taking manual segmentation by an experienced board-certificated dermatologist as reference.

In melanoma classification experiment, diagnostic features are extracted from resulting images after illumination modeling. These features are then forwarded to a linear support vector machine using a ten-fold cross validation as the training-testing strategy (Theodoridis and Koutroumbas 2006). Sensitivity (SE) and specificity (SP) are recorded to evaluate the classification performance for differentiating MM from BN. The area under the receiver operating characteristic curve (AUC) is also calculated, with a confidence interval of 95%. Classification results, computed using diagnostic features extracted from images after different illumination modeling approaches, are compared to demonstrate the goodness of the algorithms.

4.2 Lesion Segmentation

Figure 8 shows six example skin lesion images after illumination correction by different methods. It is noted that the Cavalcanti and MSIM methods cause a colour change in the shading areas, whilst the proposed method maintains a consistent chromaticity of healthy skin. This could be clearly observed in figure 8(b) and (d). Furthermore, for skin images having complex surface shapes and oversaturated illumination variations, such as figure 8(c) and (f), the Cavalcanti and MSIM methods fail to satisfactorily remove the shading effects, whilst the proposed method successfully addresses the undesired artifacts.

Based on results after illumination modeling, skin images are segmented into lesion and non-lesion areas by the same Otsu's method (Otsu 1979). Taking manual segmentation by the dermatologist as reference, the Tanimoto coefficient (*TC*) defined in (16) is adopted to quantitatively evaluate the segmentation performance (Tan *et al* 2005),

$$TC = \frac{\zeta_{manual-auto}}{\zeta_{manual} + \zeta_{auto} - \zeta_{manual-auto}} \times 100\% \tag{16}$$

where $\zeta_{manual-auto}$ denotes the number of pixels assigned to lesion areas by both manual and automatic segmentations. ζ_{auto} is the number of lesion pixels computed by automatic method, and ζ_{manual} is that selected by the dermatologist. *TC* becomes 1 if automatic segmentation is exactly the same as the manual one, whilst it is 0 when there is no overlapping between them.

Table 1 shows the segmentation accuracy carried on uncorrected and corrected skin lesion images by different algorithms. It is noted that all the methods show efficiency for correcting illumination variations and improving lesion segmentation accuracy. But compared to the state-of-art algorithms under consideration, the proposed method proved superior as well as reliable in illumination modeling, which gives the highest average *TC* value and the lowest SD in segmentation experiment.

Table 1. Comparison of segmentation accuracy on uncorrected and corrected skin lesion images by different illumination modeling methods.

	Uncorrected	Cavalcanti (Cavalcanti and Scharcanski 2011)	MSIM (Glaister *et al* 2013)	Proposed method
Average *TC* (%)	67.54	80.63	82.78	**88.96**
SD (%)	23.21	12.16	13.47	**8.13**

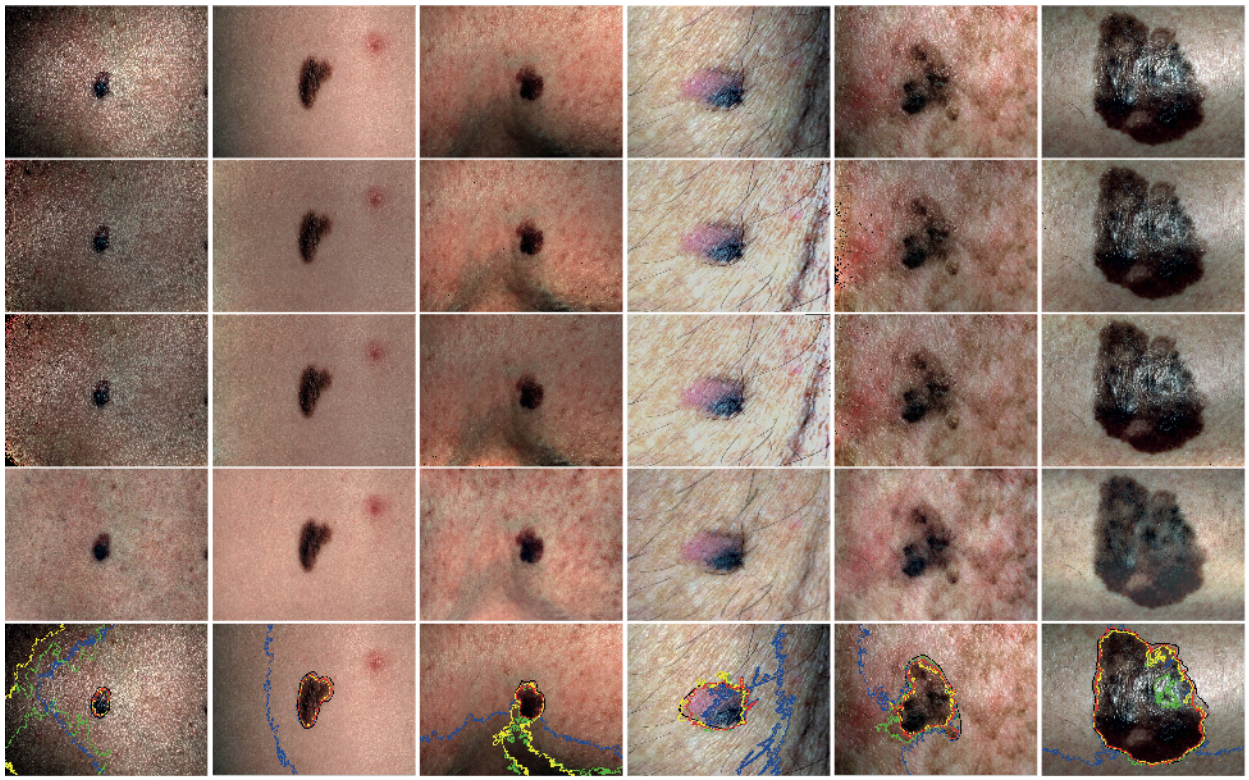

Figure 8 Comparison of different illumination modeling for skin lesion images. (1st row) Six examples from public databases (Galderma 2014, Diepgen *et al* 2014) with highlight and shading as artifacts. (2nd row) Results from Cavalcanti's method (Cavalcanti and Scharcanski 2011). (3rd row) Results from MSIM method (Glaister *et al* 2013). (4th row) Results by the proposed method. (5th row) Skin lesion segmentation on uncorrected and corrected images. Black line: manual segmentation by an experienced dermatologist. Blue line: segmentation on the uncorrected original image. Green line: segmentation on the corrected image by the Cavalcanti's method. Yellow line: segmentation on the corrected image by the MSIM method. Red line: segmentation on the corrected images by the proposed method.

4.3 Melanoma Classification

In order to demonstrate the efficiency of the chromophore indices for skin disease analysis, the present study compares the computer-aided melanoma diagnosis using diagnostic features derived from RGB colorimetry and chromophore indices. Based on widely applied ABCD rule (Friedman *et al* 1985), the diagnostic features including absolute colour variation, relative colour variation (Sun *et al* 2013), and global point signature based asymmetry measures (Liu *et al* 2012), are extracted from each skin lesion image using the existing computer-based analytical algorithms. For RGB colorimetry, these features are extracted from red, green, and blue channels as shown in (17). Whilst for chromophore indices, these features are extracted from MI and HI mappings in (18). The computed diagnostic features are normalized using a z-score transformation (Aksoy and Haralick 2001), so that 99% elements of each feature are in the range of 0~1 to prevent features of large ranges dominating the classification.

$$F_{RGB} = \{CV_{les}^{R}, CV_{les}^{G}, CV_{les}^{B}, CV_{rel}^{R}, CV_{rel}^{G}, CV_{rel}^{B}, Asy_{min}^{R}, Asy_{min}^{G}, Asy_{min}^{B}, Asy_{min+90}^{R}, Asy_{min+90}^{G}, Asy_{min+90}^{B}\} \quad (17)$$

$$F_{chrom} = \{CV_{les}^{MI}, CV_{les}^{HI}, CV_{rel}^{MI}, CV_{rel}^{HI}, Asy_{min}^{MI}, Asy_{min}^{HI}, Asy_{min+90}^{MI}, Asy_{min+90}^{HI}\} \quad (18)$$

For comparison, experiments based on RGB colorimetry, refer to the classifications using descriptors from original uncorrected images and corrected images after illumination modeling by Cavalcanti method, MSIM method and the proposed method. While experiments based on chromophore indices, are the classifications using descriptors from MI and HI mappings computed by the ICA method (Madooei *et al* 2012) and our method. The corresponding melanoma classification results are summarized in Table 2.

For classification in RGB colorimetry, the priposed method greatly increased 4~8% sensitivity and 8~21% specificity, in comparison to the results derived from uncorrected and corrected images by other methods. Moreover, sensitivity of automatic melanoma diagnosis has been further improved 12% via applying the diagnostic descriptors from chromophore indices, with 5% sacrifice in specificity. Considering that the most important objective for melanoma diagnosis is to maximize the correct recognition rate of malignant lesions, the best classification is achieved by using the chromophore descriptors from the proposed method, which gives 85.52% sensitivity, 84.07% specificity, and 84.50% overall diagnostic accuracy, respectively.

Table 2. Melanoma classification results using diagnostic features extracted from RGB colorimetry and chromophore indices.

		SE (%)	SP (%)	Acc. (%)	AUC
RGB Colorimetry	Uncorrected	65.78	68.67	67.83	0.649
	Cavalcanti (Cavalcanti and Scharcanski 2011)	69.74	76.92	74.51	0.706
	MSIM (Glaister *et al* 2013)	71.05	80.77	77.90	0.748
	Our method	73.68	**89.56**	84.88	0.867
Chromophore indices	ICA (Madooei *et al* 2012)	77.63	78.57	78.29	0.759
	The proposed method	**85.52**	84.07	**84.50**	**0.870**

5. Discussion

5.1 Comparison of Illumination Modeling Methods

In the present study, two other illumination-modeling approaches, Cavalcanti's method and MSIM method, are considered for performance comparison. It is noted that Cavalcanti and MSIM approaches cannot address highlight effects in the lesion images, while the proposed method can successfully remove this artifact. This is because both Cavalcanti and MSIM approaches refer to human skin as a merely diffuse reflectance surface, and ignore the specular reflectance in their skin models. But our method considers both specular and diffuse reflectance, so it is able to deal with highlight and shading effects in skin images of large dynamic range intensity. Hence lesion image in figure 8(f), reported fail to be

satisfactorily corrected due to highly oversaturated illumination variation (Glaister *et al* 2013), was well modeled by the proposed method. Its corresponding lesion segmentation is close to the manual one outlined by the experienced dermatologist.

Furthermore, Cavalcanti and MSIM methods make two assumptions about skin lesion images. First, skin lesion in the image is assumed illuminated by a single source of white light (Glaister *et al* 2013). Hence only V-channel in the HSV colour space is used for illumination correction. But this assumption is not always true for skin images from public databases. This is probably the reason why Cavalcanti and MSIM methods sometimes cause a colour change within the shading areas of healthy skin (figure 8 (b) and (d)). Conversely, the proposed method does not make the above assumption and corrects the illumination variations in all the RGB channels. Hence it maintains a consistent colour across homogeneous healthy skin in the corrected lesion images.

Second, both Cavalcanti and MSIM methods assume that skin lesion is found in the center of the photograph. Thus they suppose healthy skin is near the corners and borders of the image. Accordingly they use pixels in these areas to estimate the illumination map. These methods can remove shading effects when lighting variations in skin images are relatively simple (figure 8(a) and (e)). But limited pixel information poses much difficulty when characterizing skin lesion images having more complex illumination due to skin surface shapes and oversaturated variations (figure 8(c) and (f)). In comparison, our method properly describes the sophisticated lighting variations by using all the image pixels to estimate the illumination map. As a result, the proposed method gave visually superior corrected images and higher lesion segmentation accuracy during experiments. In addition, it is worth noting that the central localization assumption works only for single lesion images, such as MM diagnosis. But it is not applicable to skin images where several lesions exist, e.g. acne detection; while the proposed method proved working on this kind of skin image in our earlier study (Liu and Zerubia, 2013).

5.2 Comparison of Melanoma Classification Using RGB Colorimetry and Chromophore Indices

For classification in RGB colorimetry, melanoma diagnostic accuracy, especially specificity, greatly increases after illumination correction. This is because illumination modeling results in more accurate lesion segmentation and colour feature quantification, allowing a better distribution separation between MM and BN.

Classifications using chromophore indices largely boost the sensitivity, thanks to the melanin index and hemoglobin index properly characterizing the pathological tissue conditions of the skin (Dolotov *et al* 2004). Take melanoma image in figure 1 for example. The shape of this malignant lesion is more or less symmetric and its colour variations are relatively small in the RGB colour space. Hence it was erroneously classified as a benign naevi in the diagnostic experiments using RGB colorimetry based descriptors. In comparison, chromphore indices are physical measures. The irregular growth of melanin is generally believed as the cause of malignant melanoma. Accordingly measuring melanin distribution provides a way to evaluate the genetic instability underneath the skin surface. For this instance, pigmentation asymmetry and pigmentation variation of the lesion obviously increase in the melanin index mapping in figure 7. This leads to a correct classification using chromophore based descriptors, which categorizes the lesion as a malignant case. Hence, compared to the RGB colorimetry, chromophore indices are more efficient in describing the pigmentation distribution of the cutaneous lesions, and therefore can benefit the automatic skin disease analysis.

5.3 Limitation

The method discussed in this article was implemented in Matlab R2012b (Natick, MA, USA) on a PC with an Intel i5-4460 CPU and 8GB DDR3-1600 RAM. Since the spatial ($\sigma 1$) and intensity ($\sigma 2$) standard deviations are adaptive to every pixel in bilateral filtering, the computa- tion power for processing the algorithm cannot achieve real time. Take figure 1 with a spatial resolution of 740 × 488pixels for example. It takes 183.86s to remove highlight and shad- ing effects under the platform stated above. If a compiled language such as C++ is used, the computational time can trivially be reduced by at least an

order of magnitude. But in order to achieve real-time computation, one possible way could be to group pixels having similar intensity gradients and make them share the same spatial and intensity standard deviations during computation.

Another limitation lies in the fact that only one dermatologist's/histopathologist's evalua- tion was used to create the gold standard. As such, it is not possible to characterize inter-operator error. Although resources were not available in this study to allow for multiple experts to examine the images, in our opinion, the results still elucidate the efficiency of the proposed method for improving the quality of clinical data and assisting physicians to achieve better diagnostic results. Nevertheless, a future endeavor should strive to investigate whether the estimated error is on the order of the inter-operator error.

6. Conclusion

This paper proposes a novel illumination modeling and chromophore identification method in dermatological images for melanoma diagnosis. The derived melanin and hemoglobin indices are well identified, and prove robust to highlight and shading effects in skin colour images captured under uncontrolled imaging setting. Experiments show that the proposed method gives superior visual and segmentation results when compared to two other illumination correction approaches. Chromophore descriptors largely increase sensitivity of automatic melanoma diagnosis than those derived from RGB colorimetry. We expect that this new method will prove useful for other skin disease analysis.

Acknowledgement

This research has been conducted within the LIRA Skincare Consortium project. The first author would like to thank INRIA-DPE for funding her postdoctoral fellowship in Ayin Research Team at INRIA-SAM. Both authors are grateful for being allowed free access to the dermatological websites (Galderma S A 2014) and (Diepgen T L, Yihune G et al 2014) to perform this study. Both authors thank the reviewers for their constructive comments.

References

Aksoy S and Haralick R M 2001 Feature normalization and likelihood-based similarity measures for image retrieval *Pattern Recog. Lett.* **22** 563–82

Cavalcanti P G and Scharcanski J 2011 Automated prescreening of pigmented skin lesions using standard cameras *Comput. Med. Imag. Graph.* **35** 481–91

Claridge E, Cotton S, Hall P and Moncrieff M 2003 From colour to tissue histology: Physics-based interpretation of images of pigmented skin lesions *Med. Image Anal.* **7** 489–502

Diepgen T L, Yihune G et al 2014 Dermatology Online Atlas www.dermis.net

Dolotov L E, Sinichkin Y, Tuchin V, Utz S, Altshuler G, and Yaroslavsky I 2004 Design and evaluation of a novel portable erythema-melanin-meter *Lasers in Surg. Med.* **34** 127–35

Friedman R, Rigel D and Kopf A 1985 Early detection of malignant melanoma: the role of physician examination and self-examination of the skin *CA Cancer J Clin.* **35** 130–51

Galderma S A 2014 DermQuest http://www.dermquest.com

Glaister J, Amelard R, Wong A and Clausi D A 2013 MSIM: multistage illumination modeling of dermatological photographs for illumination-corrected skin lesion analysis *IEEE Trans. Biomed. Eng.* **60** 1873-83

Jacques S 1998 Skin optics *Oregon Medical Laser Center News*

Keller G, Lacombe V, Lee P and Watson J 2001 *Lasers in Aesthetic Surgery* (New York: Thieme) ch22

Liu Z, Sun J, Smith L, Smith M, Warr R 2012 Distribution quantification on dermoscopy images for computer-assisted diagnosis of cutaneous melanoma *Med. Biol. Eng. Comput.* **50** 503-13

Liu Z and Zerubia J 2013 Towards automatic acne detection using a MRF model with chromophore descriptors *IEEE EUSIPCO Conf. Recording* (Marrakech, 9-13 September 2013) pp 1-4
Madooei A, Drew M, Sadeghi M and Atkins M 2012 Intrinsic melanin and hemoglobin colour components for skin lesion malignancy detection *MICCAI Conf. Recording* (Nice, 1-5 October 2012) **7510** 315-22
Otsu N 1979 A threshold selection method from gray-level histograms *IEEE Trans. Sys. Man., Cyber.* **9** 62–6
Sun J, Liu Z, Ding Y and Smith M 2013 Recovering skin reflectance and geometry for diagnosis of Melanoma. In: *Computer Vision Techniques for the Diagnosis of Skin Cancer* ed J Scharcanski and M E Celebi (Berlin: Springer) ch 9 pp 243-66
Tan P, Steinbach M, and Kumar V 2005 *Introduction to Data Mining* (Boston, MA: Addison-Wesley) ch 2
Theodoridis S, and Koutroumbas K 2006 *Pattern Recognition* (Orlando: Academic press) ch 4
Thévenaz P, Blu T and Unser M 2000 *Handbook of Medical Image Processing* ed I Bankman (New York: Academic) ch 25
Tomasi C and Manduchi R 1998 Bilateral filtering for gray and colour images *IEEE ICCV Conf. Recording* (Bombay, 4-7 January 1998) pp 839–46
Tsumura N, Ojima N, Sato K, Shiraishi M, Shimizu H, Nabeshima H, Akazaki S, Hori K and Miyake Y 2003 Image-based skin colour and texture analysis/synthesis by extracting hemoglobin and melanin information in the skin *ACM Trans. on Graphics* **22** 770-9
Wandell B 1995 *Foundations of Vision* (Sunderland: Sinauer Associates) ch 4
Yamamoto T, Takiwaki H and Ohshima H 2008 Derivation and clinical application of special imaging by means of digital cameras and image freeware for quantification of erythema and pigmentation *Skin Res. Technol.* **14** 26–34.
Yang Q, Wang S and Ahuja N 2010 Real-time specular highlight removal using bilateral filtering *IEEE ECCV Conf. Record* (Greece, 5-11 September 2010) **IV** 87-100